Scanning Microscopy

Volume 1 | Number 3 Article 1

6-3-1987

Scanning Transmission Ion Microscopy as it Complements Particle Induced X-Ray Emission Microanalysis

H. W. Lefevre
University of Oregon

R. M. S. Schofield
University of Oregon

J. C. Overley
University of Oregon

J. D. MacDonald
University of Oregon

Scanning Microscopy, Vol. 1, No. 3, 1987 (Pages 879-889)
Scanning Microscopy International, Chicago (AMF O'Hare), IL 60666 USA

0891-7035/87$3.00+.00

SCANNING TRANSMISSION ION MICROSCOPY AS IT COMPLEMENTS PARTICLE INDUCED X-RAY EMISSION MICROANALYSIS

H.W. Lefevre*, R.M.S. Schofield,
J.C. Overley, J.D. MacDonald

Physics Department
University of Oregon
Eugene, OR 97403

(Received for publication March 25, 1987, and in revised form June 03, 1987)

Abstract

The early uses of Scanning Transmission Ion Microscopy (STIM) with MeV ions are reviewed. The transformation of STIM energy-loss images into maps of areal density is discussed, and is illustrated with images of a fruit fly head (Drosophila melanogaster). Freeze-dried male heads are transparent to 4-MeV protons in the dorsal and frontal directions, but in the sagittal direction the brain is opaque. STIM with molecular ions is shown to be useful for increasing contrast in low density areas. For recording registered STIM and PIXE images without changing accelerator parameters, apertures are used to accomplish the required change in beam intensity (a factor of 10^5). Molecular ions are used to assess contamination of the microbeam by scattered ions. Pixel by pixel ratios of x-ray intensity to areal density are taken to obtain maps of element concentrations. Calcium and iron maps are shown. Inner parts of the fly head are clearly seen in the concentration maps. The PIXE exposure caused differential displacements of inner parts of the head by 15 μm or less. Weight loss during the PIXE exposure was measured to be 3%.

Key Words: Scanning MeV-ion microprobe, scanning transmission ion microscopy, particle induced x-ray emission, biological microanalysis, Drosophila melanogaster, ion energy-loss spectroscopy.

* Address for correspondence:
H. W. Lefevre, Physics Department, University of Oregon, Eugene, OR 97403
Phone: (503) 686-4766

Introduction

When one uses a scanning MeV-ion microbeam or microprobe to produce and record characteristic Particle Induced X-ray Emissions (PIXE), one obtains a map or image showing the location in two dimensions of minor or trace elements in a sample. If the background matrix is non-uniform in thickness or density, one must also measure local areal densities in order to deduce areal concentrations of those elements as is discussed by Vis (1985). That is often done by recording the intensity and energy of back scattered protons at each location while the x-rays are being recorded, and then applying various analyses and corrections (Heck and Rokita, 1984; Themner and Malmqvist, 1986).

When one uses the MeV-ion microbeam (with its intensity reduced by a factor of about 10^5) to measure individual ion energy losses in transmission (Scanning Transmission Ion Microscopy or STIM) one obtains a map or image that is closely related to the areal (i.e., projected) electron density of the sample. If, as is often the case, one knows the approximate chemical composition of the sample, one can use compounded elemental stopping powers to convert energy losses into a map of areal density. STIM images can thus also provide the areal densities needed for PIXE microanalysis.

While the main purpose of this paper is to present STIM in its complementary role to PIXE, it will also become clear that the STIM images have higher resolution and lower noise, and they can be obtained much faster than PIXE images. STIM images are informative and useful in their own right. One can thus expect the use of STIM with MeV ions to increase for these several reasons.

This paper will review the early uses of STIM with MeV ions. Those uses were generally unrelated to PIXE. It will supplement that review with recent examples from our laboratory. It will discuss the transformation of energy-loss images into areal density images. Finally, it will address the problems which arise in recording registered STIM and PIXE images using apertures alone to span the required factor of 10^5 in beam intensity, and will illustrate how the breakup of molecular ions can be used as a

diagnostic tool for studying the contamination of the microbeam by scattered ions (Nobiling et al., 1975).

History

The book by Vis (1985) and the tutorial paper by Malmqvist (1986) on the applications of proton microprobes in biology and medicine each provides excellent discussions and bibliographies on PIXE microanalysis, so that subject will not be reviewed here. Neither of those works mention the use of STIM with MeV ions, however, so that history will be reviewed. The nice STIM work with ions of energy less than 100 keV (Levi-Setti and Fox, 1980) will not be included here because a connection to PIXE in that energy regime has not yet been established.

The early studies of STIM with MeV ions included work from three laboratories:

Overley et al. (1983) presented STIM images from the University of Oregon MeV-ion microprobe (Lefevre et al., 1983). Incident 3-MeV ions of H^+, He^+, and Ne^+ were used to obtain energy loss images of parts of a fruit fly (Drosophila melanogaster) and of an onion membrane. Residual ion-energy was measured with a silicon surface barrier (Si(SB)) detector. It was demonstrated that a low noise image could be obtained by using the median value of measured energies of a few (5) ions per pixel. Images were presented using a gray scale with ion energy-loss as the contrast parameter. It was later demonstrated (Overley and Lefevre, 1985) that a thickness contrast of 10 nm could be achieved with a few 3-MeV neon ions per pixel on a thin sample of unit density, and that an even higher thickness contrast might be obtained using a bolometric detector for higher resolution ion energy measurements (Overley et al., 1985).

Sealock et al. (1983) presented STIM results from the Melbourne microprobe (Legge et al., 1979). Incident 2-MeV $^4He^+$ ions were used to obtain a transmission energy-loss image of a 0.5-μm-dia latex sphere supported by a 0.4-μm-thick nylon foil. To construct that image, energy loss was used to identify those ions which had passed through the sphere. The image showed numbers of ions vs. position rather than energy loss vs. position. The Melbourne instrument has since been used to record bright field and dark field energy-loss images of diatoms with a spatial resolution of 300 nm. (Legge et al., 1986). A Si(SB) detector was used for ion energy measurements. For the dark field images, a small annular stop was used to absorb transmitted beam particles that were not scattered through a small range of angles. Thicker parts of the sample contributed proportionally more ions to the image than thinner parts did. So here, as well, numbers of ions suffering a defined energy loss rather than energy loss itself, is the contrast parameter.

Fischer (1985) has used the GSI scanning heavy - ion microscope at Darmstadt to obtain STIM energy loss images and simultaneous secondary-electron images produced by ^{16}O ions of energy 1.4 MeV/U on a fly wing. The contrast parameter in Fischer's images was again the number of ions within particular energy loss bounds.

We have here distinguished between images where the contrast parameter is numbers of selected ions from those where the contrast parameter is energy-loss of individual ions. In the former case counting statistics contribute to noise in the image. In the latter case counting statistics do not contribute to noise, as long as at least one ion per pixel is recorded.

Malmqvist (1986) has presented an address list of 24 laboratories that are involved in several aspects of MeV-ion microprobing including PIXE microanalysis. One can anticipate that a STIM capability will be added at many of those facilities since only a small additional outlay of effort and equipment is needed. The extra data collection time required for STIM is small compared to the time which must be invested to obtain a PIXE image. Finally, any sample that will survive PIXE will not be affected by STIM because the radiation dose is negligible in comparison.

STIM and Areal Density

As an example for discussion, we will use STIM data obtained from 4-MeV-H_1^+ ions incident upon the freeze-dried but otherwise unprepared heads of male fruit flies (Drosophila melanogaster). Figs. 1, 2 and 3 are, respectively, sagittal, dorsal and frontal views obtained with 4-MeV-H_1^+ ions from the University of Oregon 5-MV electrostatic accelerator. Ions from a small object aperture were focused at the sample position with an electron plasma lens (Lefevre et al. 1983, 1985) with a nine-fold demagnification. The focused beam was rastered by electrostatic deflection under computer control over a 256x256 square array of pixels. The beam was allowed to dwell at each location until an ion was detected or until 2 msec had passed. Ions were detected with a 50-mm^2 Si(SB) detector placed 1 cm beyond the sample. For each ion detected, the detector pulse height was digitized with a multichannel pulse height analyzer. Each row of the array was scanned five times, and the median value of the five measurements of pulse height at each pixel was selected and recorded by the computer. The computer generated images of Figs. 1, 2 and 3 use six gray scale levels. The six levels are adjusted so that each spans an equal number of pixels. Larger ion-energy losses correspond to whiter areas on the figures.

The central part of the head in Fig. 1 was opaque to 4-MeV-H_1^+ ions. The dorsal view of Fig. 2, however, is transparent almost everywhere. Fig. 2, shows that it is the alignment of the dense or retinal part of the compound eye with the optic lobes and the central brain that conspire to stop 4-MeV protons from the side. Fig. 1 suggests (correctly) that the frontal view of the detached head (Fig. 3) presents even less mass to protons than the dorsal view does; and that the frontal view is probably the best

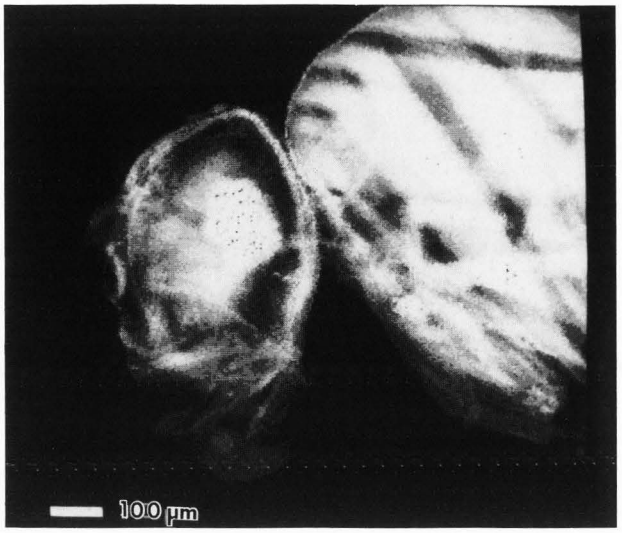

Fig. 1. 4-MeV H_1^+ STIM image of a freeze-dried male fruit fly, Drosophila melanogaster. Whiter areas indicate larger proton energy losses and higher areal densities. The central part of the head is opaque in this sagittal view.

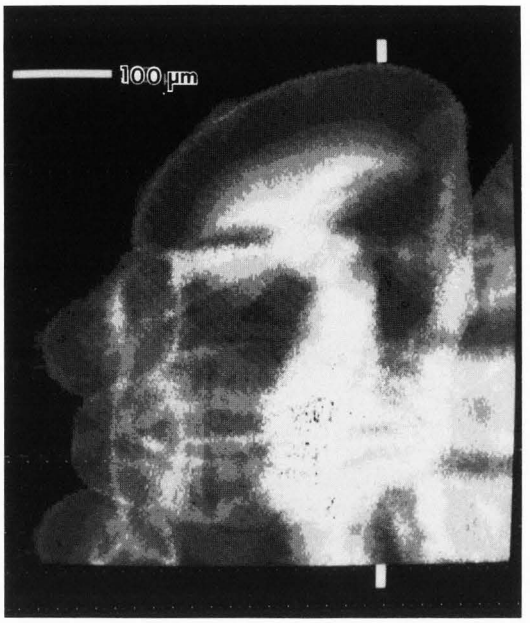

Fig. 2. A dorsal view of the head at twice the magnification of Fig. 1. The compound eye is at the top of this figure; the antennae are visible at the left. The dense central brain is transparent almost everywhere to 4 MeV protons in this view. The short vertical bars above and below locate the five scans of Fig. 5.

orientation for a PIXE study.

Where the sample is transparent to ions, one can transform measured ion energy losses into areal densities by projecting mass density, ρ, along the ion path:

$$\int \rho\, dx = \int_{Eo}^{E} \left[\frac{dE}{d(\rho x)} \right]^{-1} dE \qquad (1)$$

Extensive compilations of mass stopping powers, $dE/d(\rho x)$ (Janni, 1982), and closely related atomic stopping cross sections (Anderson and Ziegler, 1977) exist for the elements. At energies above 100 keV or so, stopping powers for compounds (or mixtures) may be accurately calculated using Bragg's rule which states that the total spatial rate of energy loss in a medium is simply the sum of the rates due to the constituent elements. For mass stopping powers, Bragg's rule becomes:

$$\frac{dE}{d(\rho x)} = \sum_i \frac{n_i A_i}{M} \left[\frac{dE}{d(\rho x)} \right]_i \qquad (2)$$

where n_i and A_i are, respectively, the number of atoms per molecule and atomic mass of the ith element, and M is the molecular mass of the compound. Thus, if the composition is known, the integral for areal density may be tabulated for a particular incident ion energy, E_o, in terms of the transmitted energy, E. The mapping from energy loss to areal density can then be accomplished for each pixel by interpolating in the table.

Fig. 4 shows areal density vs. energy loss

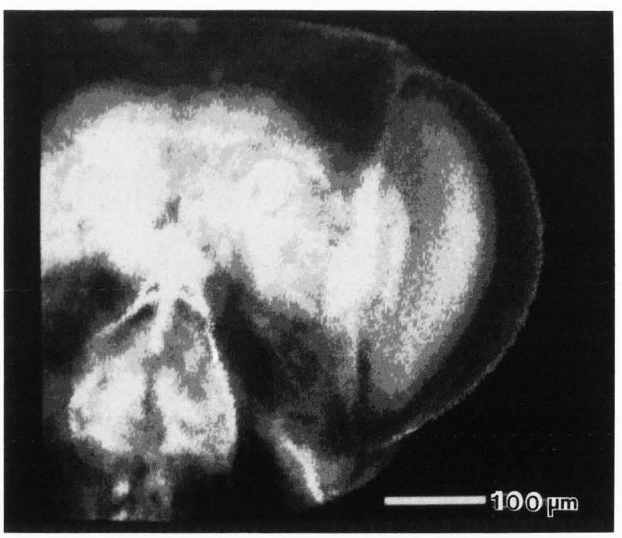

Fig. 3. Like Fig 2, but a frontal view of a detached head. The compound eye is at the right; mouth parts at the bottom. The areal density is smallest in this orientation, and it is thus the orientation of choice for a PIXE study.

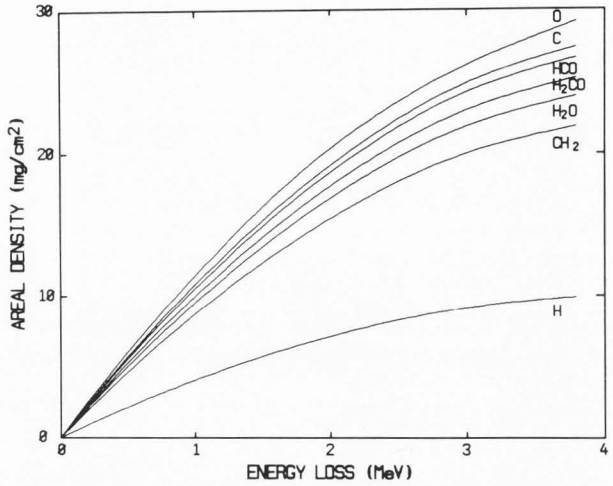

Fig. 4. Areal density vs. energy loss for 4-MeV protons in a variety of mixtures which span the stoichiometry of biological materials. Most biological material will fall between the HCO and H_2CO curves.

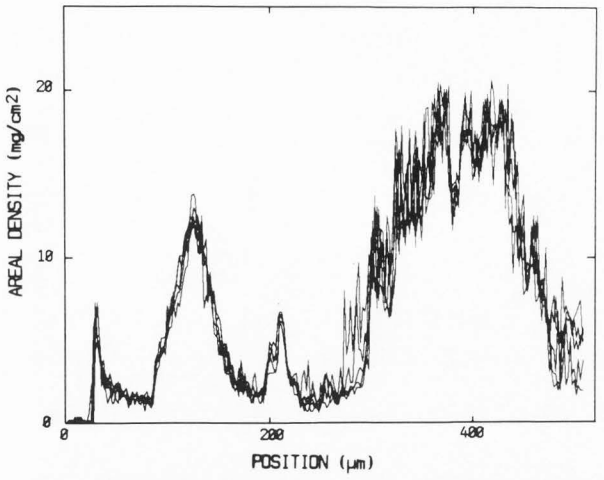

Fig. 5. Areal density vs. position for five adjacent scans across the fruit fly head. The short bars above and below Fig. 2 identify the five columns superimposed here. The top of Fig. 2 is the position origin here.

for 4-MeV protons incident on a number of combinations of H, C and O which span the stoichiometry of biological specimens. It is evident from Fig. 4 that measured energy loss can be converted to areal densities with an accuracy of about ±10% with only an approximate knowledge of composition. Other examples of insensitivity to composition in biological materials are found in calculations of ranges in various materials. In moist human muscle tissue the range of 4-MeV protons is 25 mg/cm^2 while in human bone it is 27 mg/cm^2 (Janni, 1982). The curve for tissue equivalent gelatin (Themner and Malmqvist, 1986), which we approximate by $C_5H_9O_2N$, would fall between those for HCO and H_2CO in Fig. 4 and a range of about 26 mg/cm^2 would be inferred.

Fig. 5 shows areal density vs. position for five adjacent vertical columns across the image of Fig. 2, assuming a composition $C_5H_9O_2N$. This emphasizes the quantitative nature of the image data and shows that an image made with only 6 gray scale levels hides much of the information content of the data set. Integrals of such areal density curves over the entire freeze-dried head gave a total mass of 21μg.

Precision in the energy loss measurement is determined by a convolution of the incident beam energy distribution, detector response, and longitudinal energy straggling. Incident beam energy spread is typically several keV. The resolution of a surface barrier detector is typically about 20 keV for MeV protons. Bohr theory can be used to estimate the width of the straggling distribution. For 4-MeV protons losing 2 MeV in carbon, this width is about 40 keV and it scales as the square root of areal density.

Spatial resolution at any depth is determined by a convolution of the lateral distribution of incident beam intensity and transverse straggling. The former is affected by object aperture size, lens aberrations, time varying stray fields, mechanical vibrations, and scattering from apertures and residual gas in the beam transport system. These factors limit present microprobes to spatial resolutions of order 0.1 μm, and limit us to about 2 μm.

Transverse straggling is caused by accumulated small angle coulomb scattering which introduces an increasing angular spread as the ions move through the sample. The distribution can be characterized by an rms scattering angle, as derived for example by Fermi (Fermi, 1950). Fig. 6 is a graph showing the cumulative increase in θ_{rms} as protons slow-down in carbon (Wylie et al., 1970). One can conclude that the degradation in transverse resolution by small angle coulomb scattering is only several percent of the actual sample thickness even for large energy losses.

Because a number of factors contribute to spreads in ion energy loss and transverse position, the distributions describing them will tend to be Gaussian. In such cases, selecting a median value of energy from a number of measurements will tend to select the most probable value. Unlikely events in the wings of the distributions are discarded. This effectively improves both areal density and transverse spatial resolution. It also serves to reduce noise as long as spurious events are relatively unlikely. Note that this is distinctly different from constructing an average which still includes unlikely or spurious events.

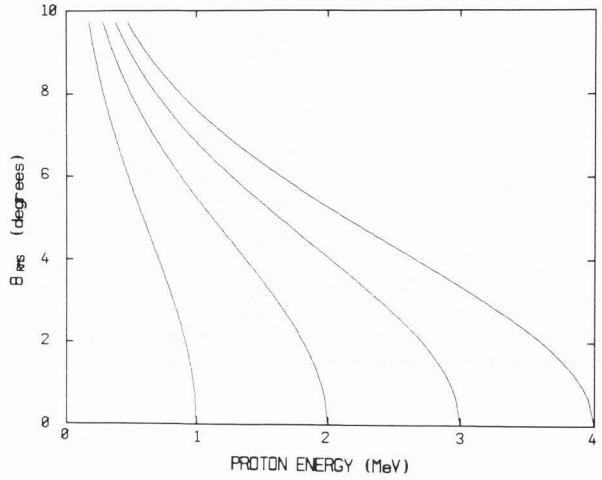

Fig. 6. Cumulative increase in the root-mean-square scattering angle as protons of four incident energies slow down in carbon. (Wylie et al., 1970).

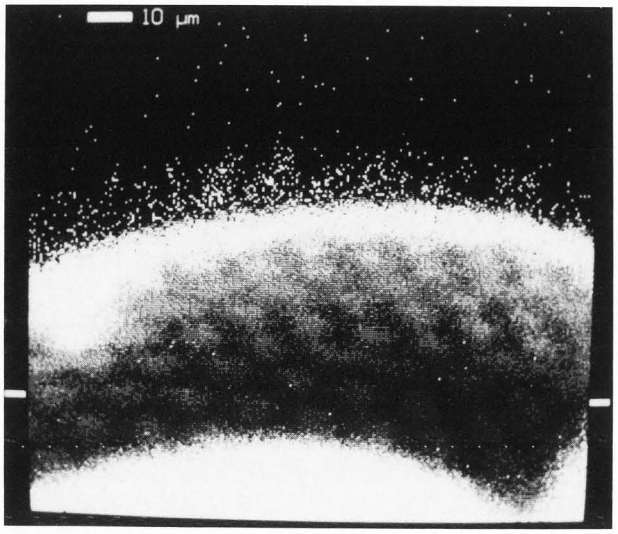

Fig. 7. 4-MeV-H_2^+-dorsal STIM image of the low density region of the compound eye, near the top in Fig. 2. H_2^+ ions were used to increase contrast. The gray scale levels have been set for best visibility of the eye lenslets, and ommatidial bristles.

STIM with Molecular Ions

The areal density just beneath the surface of the Drosophila eye in Fig. 2 is seen in Fig. 5 to be small. In order to increase the contrast in a study of that area, 4-MeV H_2^+ molecular ions were used. Those ions dissociate when they encounter matter, but both ions proceed through the sample where they are detected in coincidence in the Si(SB) detector, and their energies add. Fig. 7 is an image of the eye obtained with 4-MeV H_2^+ ions (compare with Fig. 2). The gray scale has been set for best visibility of the eye facets. Fig. 8 shows areal density for three adjacent rows between the bars in Fig. 7. The areal density contrast across the facets is about 0.4 mg/cm^2. Note that the stopping power appropriate for 4-MeV H_2^+ ions is that of 2-MeV protons, and that the ion range is only about 8 mg/cm^2 in biological material.

Fig. 9 shows three superimposed pulse height spectra from a much simpler target than a fruit fly head. Beams of 4-MeV H_1^+, H_2^+, and H_3^+ ions were rastered across a nickel grid, and STIM images were recorded. In the figure, spatial information is suppressed and only superimposed pulse height spectra of the transmitted ions are shown. Again, the molecular ions break up upon entering the grid, but the parts are detected as sums in the detector. The increased energy loss, or contrast, for H_2^+ and H_3^+ ions over H_1^+ ions is caused by the higher stopping power for the 2-MeV protons from H_2^+, and for the 1.33-MeV protons from H_3^+. We note here, in passing, that the pulse height distribution contains much information about the sample even in the absence of any explicitly spatial information. The ratio of open to obstructed area is contained in the ratio of full energy to degraded energy events. Such

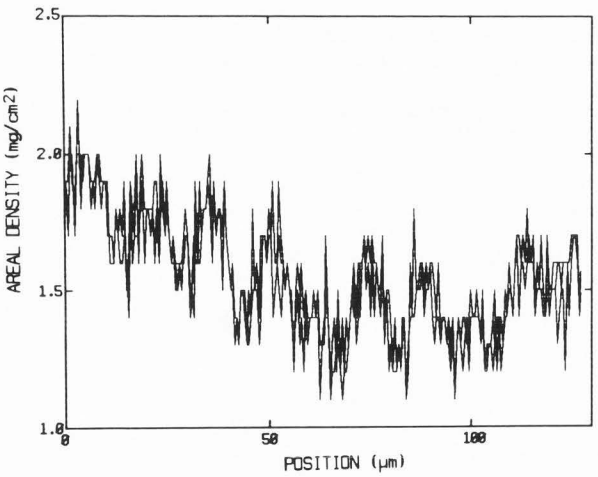

Fig. 8. Areal density vs. position for three adjacent horizontal rows through Fig. 7 as indicated there by bars. The lenslets present an areal density of about 0.4 mg/cm^2 to the beam.

measurements on a 100-nm thick sample could distinguish between ion paths a few nm apart on the basis of energy loss alone even though such spatial resolution is not available today with MeV ions.

From the above, it should be clear that molecular hydrogen ions are useful for changing contrast. We are able to change ion species quickly (minutes) because the duo-plasmatron ion

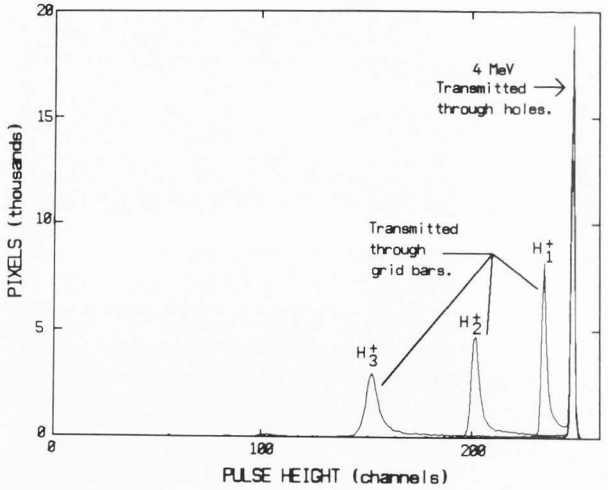

Fig. 9. Superimposed residual energy distributions of 4-MeV-H_1^+, $-H_2^+$ and $-H_3^+$ ions scanned across a nickel grid. When combined with the spatial coordinates of the pixels, each data set yields a gray scale image of the grid. The ratio of open area to obstructed area is equal to the ratio of areas in the energy distribution.

source in our single-ended accelerator delivers all three species to the analyzing magnet. To change ion species requires only a change in the current to the analyzing magnet. Since in our microprobe all elements following the object aperture are electrostatic, no changes in steering or lens strength are required. All ion species steer, raster and focus identically. (A small misregistration of images does appear when the ion species is changed. It probably is caused by different deflections in residual magnetic fields).

Apertures and Aperture Scattering

The first problem that must be addressed if one is to obtain registered PIXE and STIM images is that of dynamic range. The number of ions per pixel needed for a PIXE image of reasonable statistical accuracy is at least 10^7 times larger than the number per pixel needed for a low noise STIM image. One would like to accommodate that dynamic range without changing the operating parameters of the ion accelerator in order to avoid changes in beam steering and in ion beam stability. The range of beam intensity becomes 10^5 if one is willing to spend ten times as long accumulating PIXE data from 1/10 as many pixels. One first adjusts the accelerator to deliver an adequate intensity for PIXE. One then substitutes smaller apertures for STIM.

Nobiling et al. (1975) have given an expression for target current for a microprobe with two adjustable apertures a distance D meters apart:

$$I = \left[k \frac{I_o}{\epsilon_a^2} \right] \left[A_o \right] \left[\frac{A_a}{D^2} \right] \qquad (3)$$

Here, kI_o/ϵ_a^2 is the beam current density in units of Amperes per (meter radian)^2, and A_o and A_a are the areas in m^2 of the object and acceptance apertures, respectively.

For our microprobe, D is 3.35 m. The quantity (kI_o/ϵ_a^2) is set to about 0.75 μA (mm mrad)$^{-2}$ for PIXE. Then, with a 50-μm-dia object aperture and a 1 mm^2-acceptance aperture, PIXE beam current is 120 pA on a 6-μm-dia focal spot.

For STIM, a 10-μm-dia object aperture is selected, and the acceptance aperture is closed to 20 μm x 20 μm. The ratio of the PIXE to STIM currents is then

$$\frac{\left[A_o A_a \right]_{PIXE}}{\left[A_o A_a \right]_{STIM}} = 6.25 \times 10^4 \qquad (4)$$

Finally, we partially close the object aperture by shadowing it with a micrometer anvil and that provides a fine adjustment of beam current to give a few thousand ions per second for STIM.

In order to minimize contamination of the microprobe beam by aperture scattered ions, Nobiling et al. (1975) used highly polished and specially shaped jaws to form pairs of slits. Fischer (1985) used highly polished cylinders with their axes perpendicular to the beam to form pairs of slits. In both cases, the design goal was to minimize the "zone of transparency" at the slit surfaces. Legge et al. (1979), on the other hand, have used commercial platinum electron microscope (EM) apertures as object apertures, and we do also.

The range of 4-MeV protons in platinum is 40 μm. A 10 μm dia commercial platinum EM aperture is 3 μm thick at the edges, and the taper is such that the platinum thickness becomes equal to the ion range at a distance of 30 μm from the aperture axis. Thus, approximately 36 times as many ions with varying energy loss pass through the platinum as through the hole. The rms scattering angle of 4-MeV protons transmitted through 3 μm of platinum is 0.077 rad and the rms angle increases with the square root of the platinum thickness. For STIM the half angle subtended by our acceptance aperture at the object aperture is 3×10^{-6} rad. The fraction of scattered ions that pass through the acceptance aperture is given by ratio of the squares of those angles. The rejection ratio for scattered ions is thus 6×10^8 or larger. If hydrocarbons have deposited upon aperture edges, however, scattering angles are much smaller, and contamination of the microbeam can become severe.

In order to verify that contamination by scattered ions is small, molecular ions can be used (Nobiling et al., 1975). If molecular ions break-up upon distant apertures, it is highly unlikely that all parts of any one molecular ion will reach the detector. Thus contamination of

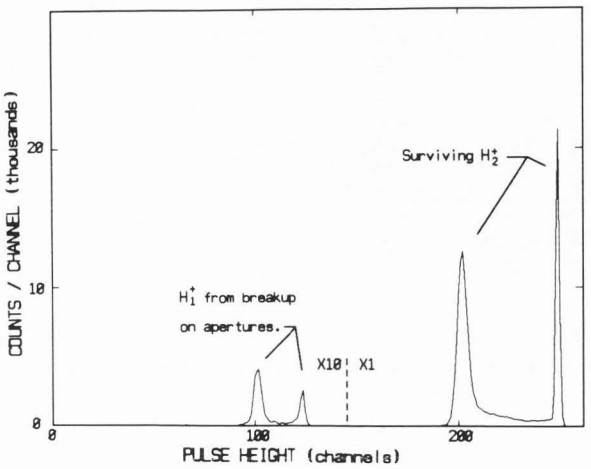

Fig. 10. Pulse height distribution from an H_2^+ beam rastered across a nickel grid. The half energy events are protons from molecular ion breakup on distant apertures. Such contamination of the beam can be measured with the microprobe lens off.

the ion microbeam by slit scattered ions can be easily discerned in the pulse height spectrum even though energy losses are very small. Fig. 10 shows such contamination from 4-MeV H_2^+ ions on a nickel grid. For this figure, data were recorded without median selection since otherwise the scattered ions would have mostly been rejected. The ions that dissociate on distant apertures are overfocused by the lens so they sample all parts of the probe field of view. They produce noise in an image if they are not removed. Note that one can measure the contamination of the beam with the microprobe lens turned off so the technique can also be used with magnetic lenses.

In order to achieve this level of scattered ion rejection, we use three more stops along the beam line: First, the edges of the object aperture are shadowed with four micrometer anvils. Second, the beam pipe is blocked with a 1-mm-dia. iris diaphragm just before the acceptance aperture. Third, a 3-mm-dia. aperture in the target chamber just before the target shadows the Si(SB) detector from most scattered ions.

While it is time consuming to adjust the system for STIM, it is then quite safe to simply open the apertures for PIXE, and that can be done without delay. One must also swing the transmission detector out of the beam before opening apertures for PIXE!

STIM and PIXE - Registered Images

It is not at first clear that PIXE can be of any use at all with a sample as complicated as a Drosophila head. The x-ray production cross sections change as the protons lose energy. The self-attenuation of x-rays by the sample depends upon the mass distribution along a diagonal path to the x-ray detector. Also, the internal parts might migrate or deform under the high radiation dose required by PIXE. Nonethe-less, we proceed.

Fig. 11(a) shows areal density obtained from the data of Fig. 3 collapsed from 256x256 pixels to 64x64 pixels to overlap PIXE images. Fig. 11(b) shows areal density vs. position along three adjacent horizontal rows of Fig. 11(a), as indicated there by bars.

Fig. 12(a) is a PIXE image in calcium x-rays produced with 4-MeV protons. The data were accumulated in 3.5 h with a dose to each pixel of 2.3×10^9 protons. Fig. 12(b) is a graph of x ray yield vs. position along the same three horizontal rows as those of Fig. 11.

A comparison of Figs. 11 and 12 shows, first, that the x-rays emitted from structures within the head can be correlated with the inner structures seen in the STIM image. Second, even without analysis it is clear that the dense or retinal part of the compound eye is richer in calcium than the brain and the optic lobes.

One sees in Fig. 11(b) that areal mass density through the dense part of the eye and brain is about 10 mg/cm^2. From Fig. 4, 10 mg/cm^2 produces an energy loss of about 1 MeV. Indeed, energy losses from 0.5 to 1.5 MeV span areal densities from 5 mg/cm^2 to 15 mg/cm^2. The calcium K x-ray production cross section falls by about 20% as the proton energy drops from 3.5 to 2.5 MeV. (Mitchell and Ziegler, 1977). To within 20%, then, one can ignore the variation in x-ray production cross section with proton energy loss for calcium K x-rays in this frontal view.

If one models the fly head as a rectangular parallelepiped with dimensions 0.34 x 0.63 x 0.74 mm for frontal, dorsal, and sagittal thicknesses, respectively, the average density is 0.13 g/cm^3. The calculated attenuation of calcium K x-rays by $C_5H_9O_2N$ along a diagonal path to the x-ray detector is a maximum of 30% (Montenegro et al., 1978). To within an uncertainty of 30%, then, one can ignore the variation in calcium K x-ray absorption in the head.

Within the uncertainty introduced by the approximations above, the calcium concentration averaged along the beam direction is proportional to the ratio of x-ray yield to areal mass density.

Fig. 13(a) shows the pixel by pixel ratio of Fig. 12(a) to Fig. 11(a). Fig. 13(b) is a graph of the ratio vs. position for the three slices used in Figs. 11(b) and 12(b). Fig. 13(b) shows that the calcium concentration in the dense part of the compound eye is about twice that in the brain. Except for thin regions which are mainly cuticle, the eye appears to stand out in calcium concentration, perhaps because of the importance of calcium in vision (Pak and Grabowski, 1978).

Fig. 14(a) is a PIXE image in iron K x-rays, and Fig. 14(b) is a pixel by pixel ratio of K x-ray yield to areal density. Here, the iron rich features seen in the image cannot be assigned to localized regions of the head on the basis of this one image alone. With similar

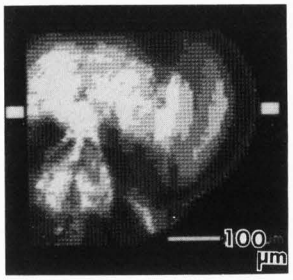

Fig. 11(a). The STIM image from Fig. 3 collapsed to 64x64 pixels for overlap with PIXE images. Three adjacent rows indicated by the bars are shown as superimposed areal density graphs in Fig. 11(b).

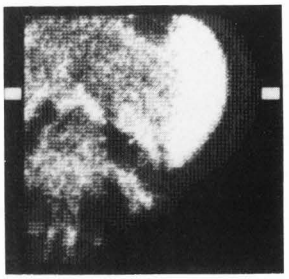

Fig. 12(a). Frontal PIXE image of the head in Ca X-rays stimulated by 4-MeV incident protons.

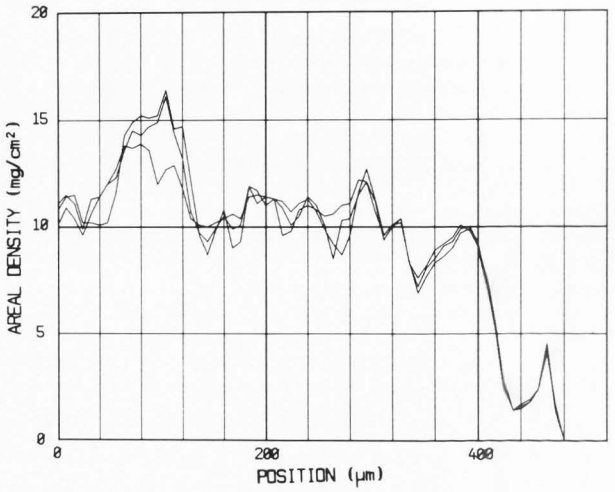

Fig. 11(b). Three adjacent rows from Fig. 11(a) plotted as superimposed graphs of areal density vs. position.

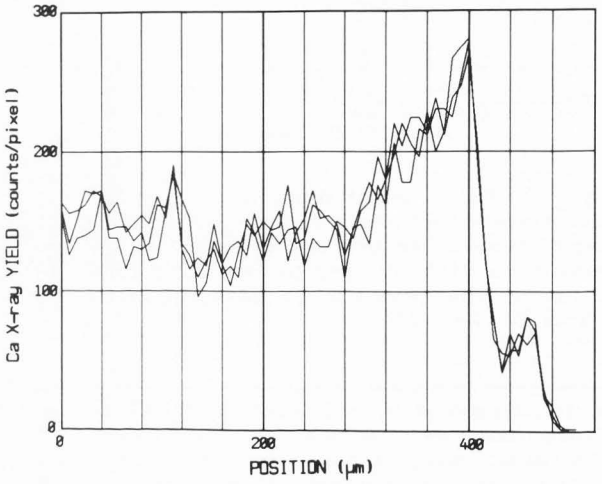

Fig. 12(b). Three adjacent rows from Fig. 12(a) plotted as superimposed graphs of X-ray yield vs. position.

Fig. 13(a). The pixel by pixel ratio of Fig. 12(a)/Fig. 11(a). The ratio is approximately proportional to Ca concentration.

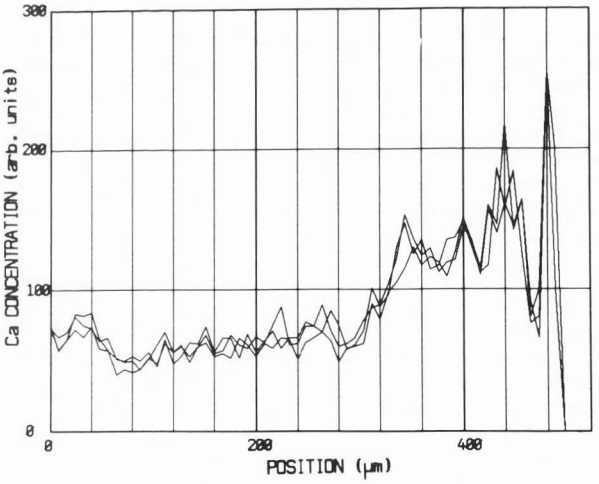

Fig. 13(b). Three adjacent rows from Fig. 13(a) plotted as superimposed graphs of Ca concentration vs. position. Ca concentration in the brain is about half that in the compound eye.

data from other orientations, however, such features might prove to be localized. Such PIXE work might thus contribute to the study of magnetoreception in organisms (Kirschvink et al., 1985).

A second STIM image like that of Fig. 3 was recorded after the PIXE exposure. The "before and after" images showed differential displacement of inner parts of the head by as much as 15 μm. Almost everything moved by 8-μm in various directions. The pixels in Figs. 11-14 are 8 μm square so all features probably moved about one pixel during the PIXE exposure. The weight loss obtained from the two STIM data sets was 3%.

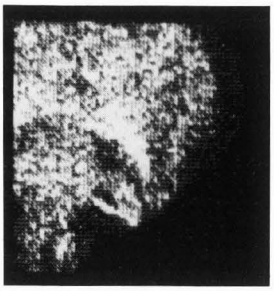

Fig. 14(a). Like Fig. 12(a) but a PIXE image in Fe X-rays.

Fig. 14(b). Like Fig. 13(a) but showing Fe concentration vs. position.

Summary

We have illustrated the use of STIM in conjunction with PIXE microanalysis to obtain approximate elemental areal concentration of an extended biological sample. The approximations involved neglect of the variation of the x-ray production cross section with ion energy loss and the neglect of x-ray absorption within the sample. In order to correct for those effects, one needs at least to know the density distribution along the ion beam path and along the x-ray path. To determine those distributions, one could envisage the use of computer assisted tomography (CAT) on STIM images taken with several sample orientations. Since STIM is a high efficiency technique, the data collection problem appears to be tractable. Unfortunately, PIXE data in several orientations would probably also be needed.

Acknowledgements

This work was supported in part by NSF grants numbered PHY 83-06683 and PHY 86-09959.

References

Anderson HH, Ziegler JF (1977) Hydrogen Stopping Powers and Ranges in All Elements. Pergamon Press, New York, 1-312.

Fermi E. (1950). Nuclear Physics. University of Chicago Press, Chicago, 30-37.

Fischer BE (1985) The scanning heavy ion microscope at GSI. Nucl. Instr. Meth. B10/11, 693-696.

Heck D, Rokita E (1984) Local matrix mass thickness determination in scanning micro PIXE by proton backscattering. Nucl. Instr. Meth. B3, 259-262.

Janni JF (1982) Proton range-energy tables, 1 keV-10 GeV. Atomic Data and Nucl. Data Tables, 27, 147-529.

Kirschvink JL, Jones DS, MacFadden BJ (eds) (1985) Magnetite Biomineralization and Magnetoreception in Organisms. Plenum Press, New York, 1-2, ff.

Lefevre HW, Connolly RC, Sieger G, Overley JC (1983) Scanning MeV-ion microprobe for light and heavy ions. Nucl. Instr. Meth. 218, 39-42.

Lefevre HW, Connolly RC, Xi DP, Sieger GE, Overley JC (1985) Can an electron plasma lens produce sub-micrometer size focal spots of MeV ions? Nucl. Instr. Meth. B10/11, 707-712.

Legge GJF, McKenzie CD, Mazzolini AP (1979) The Melbourne proton microprobe. J. Microscopy 117, 185-200.

Legge GJF, McKenzie CD, Mazzolini AP, Sealock RM, Jamieson DN, O'Brien PM, McCallum JC, Allan GL, Brown RA, Colman BA, Kirby BJ, Lucas MA, Zhu J, Cerini J (1986) Microbeam imaging at micron and submicron resolution. Nucl. Instr. Meth. B15, 669-674.

Levi-Setti R, Fox TR (1980) High resolution scanning ion probes: Applications to physics and biology. Nucl. Instr. and Meth. 168, 139-149.

Malmqvist KG (1986) Proton microprobe analysis in biology. Scanning Electron Microsc. 1986; III: 821-845.

Mitchell IV, Ziegler JF (1977) Ion Beam Handbook for Material Analysis. J.W. Mayer and E. Rimini (eds). Academic Press, NY, 392.

Montenegro EC, Baptista GB, Duarte PWEP (1978) K and L x-ray mass attenuation coefficients for low-Z materials. Atomic Data and Nucl. Data Tables 22, 131-133.

Nobiling R, Civelekoglu Y, Povh B, Schwalm D, Traxel K (1975) Collimation of ion beams to micrometer dimensions. Nucl. Instr. Meth. 130, 325-334.

Overley JC, Connolly RC, Sieger GE, MacDonald JD, Lefevre HW (1983) Energy-loss radiography with a scanning MeV-ion microprobe. Nucl. Instr. Meth. 218, 43-46.

Overley JC, Lefevre HW (1985) Precision in neon ion energy loss measurements with a silicon surface barrier detector. Nucl. Instr. Meth. B10/11, 237-240.

Overley JC, Lefevre HW, Nolt IG, Radostitz JV, Predko S, Ade PAR (1985) Bolometric detectors as ion energy spectrometers. Nucl. Instr. Meth. B10/11, 928-930.

Pak WL, Grabowski SR (1978) Physiology of the visual and flight systems. In: The Genetics and Biology of Drosophila, MA Ashburner and TF Wright, eds., Academic Press, NY, 2a, 553-583.

Sealock RM, Mazzolini AP, Legge GJF (1983) The use of He microbeams for light element x-ray analysis of biological tissue. Nucl. Instr. Meth. 218, 217-220.

Themner K, Malmqvist KG (1986) Determination of local areal densities of heterogeneous biological samples by elastically backscattered protons in PIXE microanalysis. Nucl. Instr. Meth. B15, 404-406.

Vis RD (1985) The Proton Microprobe: Applications in the Biomedical Field. CRC Press, Boca Raton, FL, 1-197.

Wylie WR, Bahnsen RM, Lefevre HW (1970) Differential excitation curves from thick target neutron spectra. Nucl. Instr. Meth. 79, 245-250. (The data for our Fig. 6 were obtained from eqn. 8 of this reference.)

Discussions with Reviewers

G.J.F. Legge: What do you see as the relative merits of STIM and backscattering for density normalization, especially with the thin specimens often used with PIXE?

K. Malmqvist: In the summary you state that a knowledge of the density distribution along the ion beam path is required for an accurate correction to be performed and that is indeed true. However, if one assumes constant density, what improvements in accuracy would you estimate possible by actually performing corrections for slowing down of ions and x-ray attenuation in this case?

Authors: Thin specimens are often used with PIXE partly because with thick specimens backscattering cannot be as easily used for density normalization. Heck and Rokita (1984) put a limit of 2 mg/cm^2 on biological sample thickness because of resonances which occur in the backscattering cross sections with larger energy losses. Themner and Malmqvist (1986) extend this limit somewhat by using a correction that can accommodate resonances.

Aloupogiannis et al. (1987) explicitly derive the corrections for energy loss and x-ray attenuation of much thicker but homogeneous specimens when energy loss of transmitted protons is measured and used to determine areal density. In the case of the nonhomogeneous Drosophila head that we have used, the original data for the several views of the head that are presented in Figs. 1-3 can be used in projection mapping to locate the major mass concentrations in three dimensions. With that knowledge in hand, one can apply the Aloupogiannis et al. (1987) corrections to the major mass concentrations where the corrections are most needed. We cannot, however, indicate what accuracy might be obtained.

The main merits of STIM, here, are two. It yields images of much higher quality than those of either PIXE or backscattering, and it can be used with thick samples. The main merit of backscattering is that the data can be accumulated incidentally and simultaneously with the PIXE data, and are guaranteed to be in instantaneous registration.

R. Levi-Setti: As much as the measurements of areal densities obtained with the MeV STIM may be useful in correlative PIXE work, how do they compare with those obtained by other methods such as x-ray microscopy? Is the information provided by this approach unique in any way?

Authors: In an x-ray microprobe, mass determination can be made by a calculation from measured Compton and Rayleigh scattering intensity (Prins, et al. (1985)). As far as we know, however, results comparable to those in Figs. 2 and 5 of this paper have not yet been presented. It appears that the analysis of x-ray scattering data to obtain areal density will not be as straightforward as that used here, and that counting statistics will enter in the x-ray scattering case. Images obtained by x-ray transmission yield linear absorption coefficients, but not areal mass densities in general because the very strong z dependence of the cross sections set unrealistic requirements on knowledge of the specimen composition.

B. Fischer: But what about scattering from the edges of the acceptance aperture? I suspect that much more than 2 in 10^9 particles scattered there can reach the Si(SB) detector. Also, compared to 4 MeV H^+ ions, many fewer breakup particles from a 4 MeV H_3^+ beam can penetrate the slit edges and "contaminate" the beam. I would recommend that one measure the amount of scattered 4 MeV H^+ particles directly by using a nuclear track detector.

Authors: Indeed, the acceptance aperture is also a source of scattered ions which can produce noise in a STIM image. Our acceptance aperture is made from two pairs of micrometer anvils which are tungsten carbide plated, and are highly polished. In searching for a low noise condition, we often find ourselves opening the acceptance aperture slightly and shadowing the object aperture more in a process that we don't fully understand. It does converge to give low noise images as long as apertures and anvils are clean.

A nuclear track detector would allow measurement of the scattered flux, but it would not help in a search for a low noise configuration. Of more use is a small opaque target which allows scattered particles to pass by and be detected in the Si(SB) detector.

R. Levi-Setti: Does the MeV STIM provide sufficient contrast to image embedded tissue sections?

Authors: Contrast ranges from 8.5 eV/nm for 4 MeV-protons in unit density carbon to 1200 eV/nm for 4 MeV Neon ions in unit density carbon. There is probably sufficient contrast with one beam or another to image unstained embedded sections. With 4 MeV Neon ions, a 1% areal density difference would be observable in a 1 μm thick section.

K. Malmqvist. What do you think is the main contributor to the observed displacement in the specimen after PIXE analysis? Is it a temperature effect or an effect of radiation dose?

G.J.F. Legge: What was the means of mounting the specimen for PIXE measurements and was the movement observed that of the substrate or was it probably movement within the specimen? Use of a stationary spot would have tended to locally heat the specimen but that obviously depends upon the dwell time and hence upon the number of repetitions of the scan; so could you also describe the conditions of the PIXE irradiation?

Authors: The head was supported by a metal post to which it was attached with conducting epoxy cement. The dwell time of the beam was 0.2 seconds on each pixel, and the scan was repeated 15 times.

Specimen changes were probably caused by radiation rather than thermal effects. Using the thermal conduction model reported by Vis (1985) and the value of thermal conductivity of tissue used there, 10^{-4} W $(cmC^{o})^{-1}$, we obtain a

temperature rise of about 10 C^{o} along the beam path in an approximation of our geometry. However, the thermal conductivity of a freeze dried head in vacuum is not known. If, for example, the brain were thermally insulated from the post, but were in thermal equilibrium when radiation cooled, the temperature rise would be about 100 C^{o}. In either case the thermal time constant is very short compared to the dwell time.

The dose delivered to each pixel by the proton beam was about 10^{7} J/kg.

K. W. Jones: What do you think is the best way to express elemental concentrations in small hetrogeneous objects?
Authors: Let the number density of atoms of type i in a small volume element dxdydz be called n_i. Then the mass fraction of species i is given by

$$c_i = \frac{n_i A_i}{\sum_j n_j A_j} \qquad (5)$$

where A_i is the molar mass of species i, and the summation index j is over atoms of all types in the volume element. Ideally, one would measure and present $c_i(x,y,z)$. On a two dimensional map, one can measure and present $\langle c_i(y,z)\rangle$. We interpret the above question as one about the nature of the average over x, the depth of material probed by the beam.

In the particular case where c_i is independent of x, but the density is not, one can write out in terms of the number of counts C_i in the X-ray detector

$$c_i = \frac{C_i A_i}{N_p \int_0^T \sigma_i(x) N_A \epsilon_i(x) \rho(x) dx} \qquad (6)$$

where $\sigma_i(x)N_A$ is the depth dependent molar x-ray production cross section (N_A is Avogadro's number); $\epsilon_i(x)$ is the probability that an emitted X-ray will yield a count in the X-ray detector; N_p is the number of incident protons, and $\rho(x)$ is the specimen density. Since STIM measures $\int_0^T \rho(x)dx = \langle \rho T \rangle$ (see eqn. 1), one must use a stopping power weighted average of $\sigma_i(x)\epsilon_i(x)$ in order to correctly recover c_i. If

$$\langle \sigma_i \epsilon_i \rangle = \frac{\int_{E_o}^{E} \frac{\sigma_i \epsilon_i dE}{dE/d(\rho x)}}{\int_{E_o}^{E} \frac{dE}{dE/d(\rho x)}} \qquad (7),$$

then

$$c_i = \frac{C_i A_i}{N_p \langle \sigma_i N_A \epsilon_i \rangle \langle \rho T \rangle} \qquad (8).$$

In this paper we have presented relative concentrations rather than the absolute concentrations described by equation 8 because we had not yet measured ϵ, the extrinsic detector efficiency, when the paper was prepared.

R. Levi-Setti: Beyond the demonstration phase of the method, have combined STIM-PIXE observations been employed in actual research applications?
Authors: No. Not yet.

Authors: An important question in our minds has been on reproducibility of the PIXE/STIM ratios. Since this manuscript was prepared, we have repeated these measurements with essentially the same results. We have also corrected the calcium measurements for interference by potassium, and find that the ratio of calcium concentration in the eye to that in the brain is nearer to four than to two. The cuticle signal also decreased, and was mainly caused by potassium rather than calcium.

Supplementary References:

Aloupogiannis P, Robaye G, Roelandts I, Weber G (1987) An improved method for matrix effects corrections using the energy loss determined along with the PIXE measurements. Nucl. Instr. Meth. B22, 72-77.

Prins M, Dries W, Lenglet W, Davies ST, Bowen K (1985) Trace element analysis with synchrotron radiation at SRS Daresbury. Nucl. Instr. Meth. B10/11, 299-302.